Control Engineering Practice 173 (2026) 106981

Contents lists available at ScienceDirect

Control Engineering Practice

journal homepage: www.elsevier.com/locate/conengprac

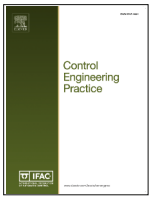

Data-driven disturbance compensation for core-type linear motors using TISO-GPR integrated with disturbance observers ⋆

Hanul Jung [a], Hoyeong Yeo [b], Hamin Chang [c], Sehoon Oh [b,*]

[a] Mobility AI Convergence Research Section, ETRI, Daegu, Republic of Korea
[b] Department of Robotics and Mechatronics Engineering, DGIST, Daegu, Republic of Korea
[c] Elmore Family School of Electrical and Computer Engineering, Purdue University, Indiana, United States

ARTICLE INFO

Keywords:
Gaussian process regression
State-dependent disturbance
Data-driven disturbance compensation
Disturbance observer
Model mismatch

ABSTRACT

An integrated control structure that combines Gaussian process regression (GPR) and a disturbance observer (DOB) is proposed for a core-type linear motor that is affected by patterned disturbance and model mismatch. The conventional controller is a DOB-based feedforward/feedback structure, and the compensation performance is limited by the fixed bandwidth of the Q-filter and the estimation bias that appears under model uncertainty. In addition, the effective frequency is shifted by the motion velocity, and disturbance rejection is degraded under a fixed-bandwidth design.

A two-input single-output GPR (TISO-GPR) that uses the position and the velocity as inputs is designed to model a lumped disturbance. A periodic kernel is applied on the position axis to represent the spatial period, and a kernel that reflects the velocity-dependent disturbance component is applied on the velocity axis, where the spatial period is fixed by the device geometry and consistent prediction on the position axis is enabled beyond the training range. The disturbance estimated by the DOB is used for training, and the posterior mean estimate is used as the compensation signal in the feedback loop, which is inserted as an internal feedback compensation signal within the DOB-based structure. A time-domain analysis shows that the compensation is bounded and that a small-gain condition guarantees BIBO stability. Experiments confirm that the proposed method improves the tracking performance and robustness.

1. Introduction

Core-type linear motor stages are widely used in semiconductor, display, and precision manufacturing equipment, and high thrust density and strong mechanical rigidity are considered advantages (Gao et al., 2023; Li et al., 2017). The thrust is generated by the interaction between the iron core in the mover and the permanent magnets that are placed at periodic intervals (Ahmed et al., 2019; Yang & Zhou, 2023). However, this structure produces patterned disturbances that include a position-dependent repetitive component and additional variations that change with the operating condition (Wang et al., 2023). Industrial systems require a long stroke, high speed, and micrometer-level tracking accuracy, and the control bandwidth and robustness are treated as key performance measures (Wang et al., 2024). Under these requirements, the patterned disturbance and the model uncertainty of core-type linear motor stages remain factors that limit the control performance.

The target disturbance consists of a position-based periodic component and a velocity-dependent component (Liu et al., 2023; Tan et al., 2004). Under constant velocity, the position-based component is observed as a repetitive pattern in the time domain, and the period becomes shorter as the velocity becomes higher (Yang & Zhou, 2023). In acceleration and deceleration intervals, the effective frequency and the amplitude vary at the same time, and a nonlinear shape appears. In the position domain, the spatial period remains constant, while in the velocity domain, the disturbance shows a slow trend that depends on the velocity (Sasaki et al., 2024). Because of this dual property, the effective frequency of the disturbance moves with the velocity, and compensation becomes difficult under a fixed-bandwidth controller, and the control error increases when a model mismatch exists.

Repetitive control (RC), iterative learning control (ILC), and periodic DOB are widely used to remove periodic disturbances (Aarnoudse et al., 2024; Cho & Nam, 2021; Rogers et al., 2024). RC suppresses the

⋆ This work was supported by Electronics and Telecommunications Research Institute (ETRI) grant funded by the Korean government [26ZD1160, Advancement and Commercialization of Daegu-Gyeongbuk Regional Strategic Industries (Robots, Mobility, AI, Medical, etc.)], by the National Research Foundation of Korea (NRF) grant funded by the Korea government (MSIT) (No. RS-2024-00354028), and by Basic Science Research Program through the National Research Foundation of Korea (NRF) funded by the Ministry of Education (No. RS-2025-25420118) (Hanul Jung and Hoyeong Yeo contributed equally to this work.)

* Corresponding author.
E-mail addresses: hanul@etri.re.kr (H. Jung), sehoon@dgist.ac.kr (S. Oh).

https://doi.org/10.1016/j.conengprac.2026.106981
Received 30 November 2025; Received in revised form 24 February 2026; Accepted 26 March 2026
Available online 5 April 2026

fundamental period and its harmonics based on the internal model principle (Aarnoudse et al., 2024), and a high rejection gain is achieved when the reference period and the sampling are synchronized. ILC corrects the trial error in repeated tasks or identical trajectories and achieves precise tracking (Tsurumoto et al., 2024). Periodic DOB uses position synchronization and phase information so that the disturbance estimation of the DOB is reinforced in a periodic manner (Li et al., 2022). However, these approaches assume a fixed period and a reference profile, and the compensation can fall outside the effective band when the velocity changes and the effective frequency moves. Sensitivity to model mismatch and reference variation also remains. Therefore, data-based disturbance compensation is required that can address velocity change and model uncertainty while the basic control structure is kept.

Data-based compensation has been studied to estimate and cancel specific disturbances while maintaining the conventional control structure. High-order function fitting provides reasonable performance (Wu et al., 2024a,b), but the method requires high design effort for model order and parameter tuning, and it is sensitive to modeling error. GPR-based compensation shows good performance (Beckers et al., 2022; Mooren et al., 2024, 2022), although the computation load can be significant, and many studies place the compensation in a feedforward path, which limits the closed-loop robustness. In recent TISO-GPR based compensation, an Squared Exponential (SE) kernel is often used as a default option (Sasaki et al., 2024). In this context, the spatial periodicity in x and the slow bias in $\dot{x}$ are treated as distinct physical properties. Therefore, a kernel is required that explicitly encodes the spatial periodicity n the motor position x and models the velocity-dependent bias in the motor velocity $\dot{x}$ separately, where x and $\dot{x}$ denote scalar state variables of the linear motor. Unlike common feedforward implementations, the GPR posterior mean is inserted as an internal feedback compensation signal within the DOB-based two-degree-of-freedom structure. In addition, boundedness of the compensation signal is characterized and a sufficient condition for BIBO stability is derived for the integrated DOB/GPR structure.

The present work keeps the original DOB-based two-degree-of-freedom control structure and adds a data-based compensation path in parallel. The disturbance is estimated by a TISO-GPR that uses the position and the velocity as inputs, where an additive kernel is constructed using a periodic kernel on x and an SE kernel on $\dot{x}$. Extrapolation on the position axis x is enabled outside the training range because the spatial period is fixed by the device geometry.

In summary, the main contributions of this paper are as follows:

1. A structure is proposed that estimates the lumped disturbance directly by a TISO-GPR that uses an additive kernel composed of a periodic kernel on x and an SE kernel on $\dot{x}$, so that the spatial period from the device geometry and the velocity dependence are reflected separately.
2. The DOB-based two-degree-of-freedom control structure is preserved, and a GPR compensation path is added in parallel with the DOB as a feedback path, so the DOB-based 2-DoF controller keeps its usability and easy tuning.
3. A BIBO stability condition is derived in the time domain based on a small-gain argument, and experiments show that the performance improvement is maintained under various operating conditions.

2. Problem formulation

2.1. Brief description of core-type linear motor stage

A core-type linear motor, as shown in Fig. 1, is widely used in precision positioning systems that require high thrust density and structural rigidity. The thrust is generated by the magnetic interaction between strong permanent magnets attached to the stationary part with an interval and the iron core inside the moving carrier that travels along the magnets.

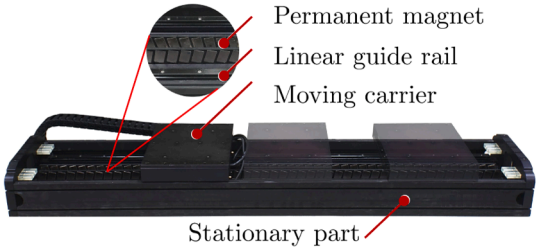

Fig. 1. Iron core-type linear motor stage.

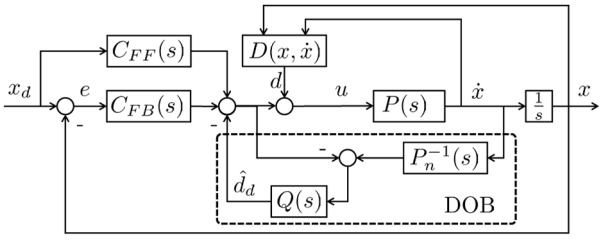

Fig. 2. Block diagram of the conventional robust model-based control.

However, a structural characteristic induces a nonlinear position-dependent disturbance that is known as cogging force. The cogging force varies with the mover position and is determined by the geometric configuration of the magnets arranged at constant intervals and the iron core. Therefore, the cogging force F_{cog} can be expressed as a static function of the position x, and it has the following periodicity:

$$F_{\text{cog}}(x) = F_{\text{cog}}(x+\tau), \tag{1}$$

where τ denotes the spatial period determined by the magnet pitch of the stator (pole pitch).

At constant velocities, the cogging force is periodic in time. When the velocity varies, it becomes nonperiodic because the passage time of the mover iron core across each magnet changes. A velocity-dependent offset is likewise observed, which is attributed to changes in flux linkage or back EMF (Sasaki et al., 2024), and the amplitude or phase of the disturbance changes accordingly. This velocity dependence distorts the waveform in time or position, and the controller performance is affected. Hence (1) is specified as follows.

$$F_{\text{cog}}(x,\dot{x}) = \alpha(\dot{x}) \cdot \sin\left(\omega_{\text{cog}}\right) + \beta(\dot{x}), \tag{2}$$

where $\alpha(\dot{x})$ denotes the velocity-dependent amplitude, and $\beta(\dot{x})$ denotes the baseline offset that represents a velocity-dependent bias, especially at high velocity, $\omega_{\text{cog}} = 2\pi x/\tau$ represents the spatial excitation determined by the mover position and the pole pitch τ.

Damping and viscous friction vary with velocity (Yang & Zhou, 2023), whereas the rigid-body parameters, including the nominal damping B_n, are treated as a constant in the nominal model. This plant/model mismatch is not estimated by the DOB, so it appears as a velocity-dependent bias in the disturbance estimate and the compensation performance is degraded (Sasaki et al., 2024).

2.2. Disturbance observer design based on frequency domain approach

Fig. 2 shows the conventional integrated control consisting of the feedback, the feedforward controllers, and the DOB. This control scheme is widely used because it maintains a simple architecture while improving tracking performance. The DOB estimates the lumped disturbance using the nominal model, and low-frequency disturbance is removed effectively inside the DOB bandwidth, although the performance is constrained by modeling error and the selection of the bandwidth.

The feedback controller C_{FB} is designed as

$$C_{FB}(s) = K_p + K_{\text{d}}s, \tag{3}$$

where K_p and K_d are proportional, derivative gain, respectively. Whereas, the feedforward controller C_{FF} is constructed from the inverse of the nominal model:

$$C_{FF}(s) = P_n^{-1}(s), \tag{4}$$

where $P_n(s)$ is the nominal model that approximates the actual plant $P(s)$, and it is represented by the rigid-body dynamics with the nominal mass M_n and the nominal damping B_n.

The DOB is composed of the nominal model $P_n(s)$ and the Q-filter. The Q-filter is designed as

$$Q(s) = \frac{\omega_q^{n_r}}{(s+\omega_q)^{n_r}}, \tag{5}$$

where ω_q is the cut-off frequency that determines the bandwidth of the Q-filter and n_r is the relative degree of the nominal model.

In Fig. 2, $x_d, x, \dot{x}$, and d denote the position command, the measured position, velocity, and the undesired disturbance, respectively. The error is defined as $e = x_d - x$ and u represent the control effort applied to the plant. The disturbance estimate $\hat{d}_d$ obtained by the DOB.

The closed-loop behavior of the conventional integrated control is given as follows:

$$G_{x_d \to x}(s) = \frac{\big(C_{FB}(s) + C_{FF}(s)\big)P(s)}{1 - Q(s) + \big(C_{FB}(s) + Q(s)P_n^{-1}(s)\big)P(s)}, \tag{6}$$

$$G_{d \to x}(s) = \frac{1 - Q(s)}{1 - Q(s) + \big(C_{FB}(s) + Q(s)P_n^{-1}(s)\big)P(s)}, \tag{7}$$

where (6) and (7) describe the transfer functions from the position reference x_d and the external disturbance d to the measured position x, respectively.

Since (5) is designed as a low-pass filter, (6) and (7) are simplified in the frequency region where $Q(s) \simeq 1$ as follows.

$$G_{x_d \to x}(s) \simeq 1, \tag{8}$$

$$G_{d \to x}(s) \simeq 0, \tag{9}$$

This result shows that the conventional integrated control removes modeling error and low-frequency disturbance effectively when $Q(s) \simeq 1$. When $Q(s) \simeq 0$, the closed-loop behavior is approximated by:

$$G_{x_d \to x}(s) \simeq \frac{(C_{FB}(s) + C_{FF}(s))P(s)}{1 + C_{FB}(s)P(s)}, \tag{10}$$

$$G_{d \to x}(s) \simeq \frac{1}{1 + C_{FB}(s)P(s)}, \tag{11}$$

where (10) and (11) indicate that the DOB does not contribute outside its bandwidth and that the disturbance rejection depends only on the feedback controller.

The effectiveness of the DOB depends on the bandwidth set by the Q-filter, and a higher cutoff frequency improves disturbance rejection at the cost of increased noise sensitivity and modeling error.

2.3. Disturbance analysis based on two domains

In this section, the disturbance estimation obtained by the DOB is analyzed in the position and velocity domains to clarify the state-dependent structure of the disturbance and to present the necessity of $(x, \dot{x})$-based compensation.

The disturbance estimation performance of the DOB is expressed as $G_{d \to \hat{d}}(s)$, which can be obtained from Fig. 2 as follows:

$$G_{d \to \hat{d}}(s) = \frac{Q(s)P(s)\big(C_{FB}(s) + P_n^{-1}(s)\big)}{1 - Q(s) + \big(C_{FB}(s) + Q(s)P_n^{-1}(s)\big)P(s)}, \tag{12}$$

when $P(s) \approx P_n(s)$ and $Q(s) \approx 1$, it becomes $G_{d \to \hat{d}}(s) \approx 1$, and the disturbance is estimated accurately. When the upper limit of the effective bandwidth of $Q(s)$ is defined as ω_Q, the spatial periodic component can be estimated sufficiently if $\omega_{\text{cog}} < \omega_Q$. On the other hand, when $P(s) \neq P_n(s)$ or $\omega_{\text{cog}} \gtrsim \omega_Q$, the estimation error increases.

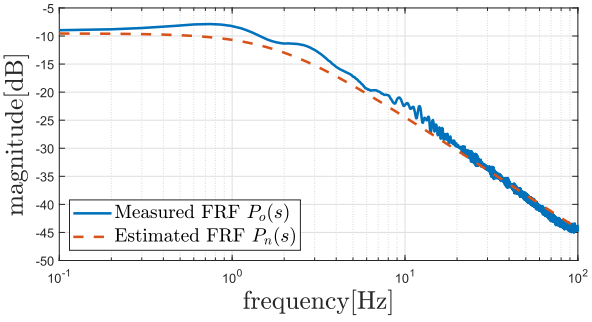

Fig. 3. Frequency response function of the core-type linear motor stage in Fig. 1.

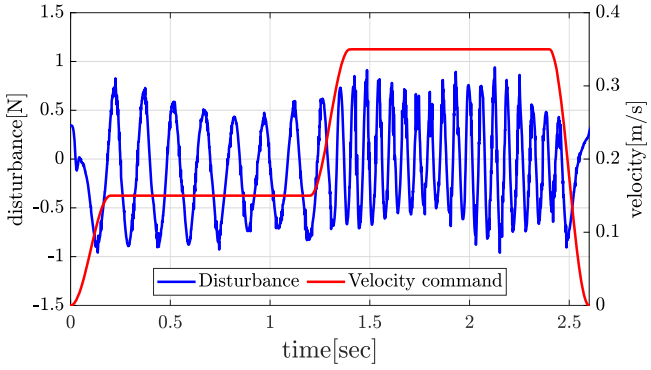

Fig. 4. Disturbance estimated by the DOB in the time domain.

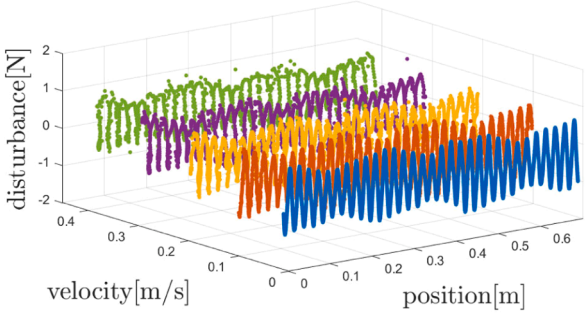

Fig. 5. Disturbance characteristics in position and velocity domains:lumped disturbance $d(x, \dot{x})$ visualized as a 3D plot.

The target system of this study, the core-type linear motor stage $P(s)$, is shown in Fig. 1, and the frequency response function of $P(s)$ is shown in Fig. 3. The nominal model $P_n(s)$ is defined as a rigid model with $M_n = 0.2621$ and $B_n = 3$. The test trajectory is designed so that the motion starts from rest and reaches constant velocities of 0.15 and 0.35 m/s, and the two constant-velocity intervals are connected smoothly with an acceleration phase. The disturbance in the time domain is shown in Fig. 4.

In the time domain, the disturbance depends on the motion condition. Under constant velocity, a repeating pattern is observed and the period becomes shorter as the velocity increases. During acceleration and deceleration, the frequency and amplitude change over time, so the disturbance becomes nonperiodic.

The disturbance in Fig. 4 is represented in the state-variable domain as the 3D distribution shown in Fig. 5. The disturbance exhibits a position-dependent repetitive pattern with a fixed spatial period, and the amplitude and offset vary with the velocity.

Therefore, the unknown disturbance can be represented by the decomposed model as

$$d(t) = d_p(x) + d_v(\dot{x}) + \epsilon(t), \tag{13}$$

where $d_p(x)$ denotes the spatial periodic component, $d_v(\dot{x})$ denotes the velocity-dependent offset component, and $\epsilon(t)$ represents the residual or modeling error, including unmodeled dynamics and DOB model mismatch. This representation can be limited when the residual deviates from a static function of $(x, \dot{x})$ under strong acceleration or contact/impact, which is outside the scope of this paper.

In the constant-velocity phase, $d_p(x)$ is dominant as a periodic signal in the time domain, and its fundamental frequency is given by $\omega(t) = 2\pi\dot{x}/\tau$. In the acceleration and deceleration phases, $\omega(t)$ varies with time, resulting in a time-varying waveform, and the influence of $d_v(\dot{x})$ becomes observable. In contrast, in the position domain, $d_p(x)$ maintains a consistent pattern because it has a fixed spatial frequency.

On the other hand, since $Q(s)$ has a fixed bandwidth, ω_{cog} exceeds ω_Q at high velocity, leading to a decrease in estimation and compensation performance. In the acceleration and deceleration phases, $\omega_{\text{cog}}(t)$ varies with time, results in difficulty in responding to time-varying characteristics in the time domain. Residual disturbance increases during the transient intervals in Fig. 4, indicating the bandwidth limitation of $Q(s)$. Therefore, the disturbance estimate obtained from the DOB can be unreliable when $\omega_{\text{cog}} \gtrsim \omega_Q$, and this operating region is treated as outside the reliable estimation range.

The disturbance of the system is represented as $d(x, \dot{x})$, which combines the position-dependent and velocity-dependent components. With a fixed-bandwidth DOB, it is difficult to simultaneously handle the frequency shift caused by velocity variation and the model mismatch. Therefore, an additional compensator utilizing both state variables as inputs is required. It is particularly important to consider the characteristics of each state variable appropriately.

3. Design of two-input single-output Gaussian process regression model

3.1. Two-input single-output Gaussian process regression based on periodic and squared exponential kernels

The GPR is a non-parametric regression method. In this study, a GPR-based disturbance model is constructed from position x and velocity $\dot{x}$ so that the composite disturbance can be learned from data. Since real-world data may contain bias, the observations are centered by subtracting the sample mean, so that a zero-mean Gaussian distribution can be assumed (Topa et al., 2015).

Let the actual disturbance be denoted as d_g, and a compensated disturbance y_g is defined by subtracting the mean of d_g so that the positive bias in the dataset is removed. Specifically, the compensated disturbance y_g is given by:

$$y_g = d_g - \text{mean}(d_g) \tag{14}$$

This transformation ensures that the distribution of the disturbances has zero mean, which is assumed during the training of the GPR model. The input of GPR is defined as a two-dimensional vector composed of position x, and velocity $\dot{x}$:

$$\mathbf{x} = [x, \dot{x}]^\top \in \mathbb{R}^2. \tag{15}$$

The output of the GPR model is the predicted compensated disturbance $\hat{y}_g$, which is obtained as:

$$\hat{y}_g = f(\mathbf{x}) + \varepsilon, \tag{16}$$

where $f(\mathbf{x})$ represents the latent function of the state-dependent disturbance, and ε is Gaussian noise with zero mean and variance σ_n^2 that includes measurement noise and residual error.

The training dataset $\mathcal{D}$ is defined as:

$$\mathcal{D} = (\mathbf{x}_i, \hat{y}_i)_{i=1}^N, \quad \mathbf{x}_i \in \mathbb{R}^2, \quad \hat{y}_i \in \mathbb{R}, \tag{17}$$

where $\mathbf{x}_i$ is the input vector composed of position and velocity, $\hat{y}_i$ is the disturbance y_g corresponding to the state $\mathbf{x}_i$, and N is the number of training dataset, respectively. Based on this dataset, the GPR model is trained, where the dataset is collected within the reliable estimation range of the DOB because the regression target is generated from the disturbance estimation of DOB.

The function $f(\mathbf{x})$ is assumed as a Gaussian process with zero mean, which is assumed after compensating for the bias in the data:

$$f(\mathbf{x}) \sim \mathcal{GP}(0, k^{\text{ps}}(\mathbf{x}, \mathbf{x}')), \tag{18}$$

where $k(\mathbf{x}, \mathbf{x}')$ is defined in an additive form to encode the dominant position- and velocity-dependent components in (13), rather than to imply exact physical independence.

$$k^{\text{ps}}(\mathbf{x}, \mathbf{x}') = k_x^{\text{pe}}(x, x') + k_{\dot{x}}^{\text{se}}(\dot{x}, \dot{x}'), \tag{19}$$

$$k_x^{\text{pe}}(x, x') = \sigma_{f,x}^2 \exp\left(-\frac{2\sin^2(\frac{\pi|x-x'|}{\tau})}{\ell_x^2}\right), \tag{20}$$

$$k_{\dot{x}}^{\text{se}}(\dot{x}, \dot{x}') = \sigma_{f,\dot{x}}^2 \exp\left(-\frac{(\dot{x}-\dot{x}')^2}{2\ell_{\dot{x}}^2}\right), \tag{21}$$

Here, $k_\bullet^{\text{ps}}$ represents the periodic kernel (PE) that models spatial periodicity, and $k_\bullet^{\text{se}}$ represents the SE kernel that models smooth changes of velocity-dependent disturbance, including friction effects and the dominant part of the residual term that appears as a velocity-dependent bias, and keeps the compensation signal bounded within the trained velocity range.

The signal variances $\sigma_{f,x}^2, \sigma_{f,\dot{x}}^2$ and the length-scales $\ell_x, \ell_{\dot{x}}$ are hyperparameters that determine the sensitivity and the local correlation structure of the data. The spatial period τ is fixed to represent the structural periodicity. Since the geometric spacing of the permanent magnets in this stage is known to be 22.5 mm, the parameter is set as $\tau = 0.0225$. This value is consistent with the spatial periodicity observed in Section 2.3.

The GPR prediction consists of the posterior mean and variance. The prediction of the compensated disturbance for $\bar{y}_*$ a given input $\mathbf{x}_*$ is given by

$$\bar{y}_* = \mathbf{k}_*^\top (\mathbf{K} + \sigma_n^2 \mathbf{I})^{-1} \mathbf{y}, \tag{22}$$

$$\text{cov}(y_*) = \mathbf{k}_{**} - \mathbf{k}_*^\top (\mathbf{K} + \sigma_n^2 \mathbf{I})^{-1} \mathbf{k}_*, \tag{23}$$

where $\mathbf{K} \in \mathbb{R}^{N \times N}$ is the kernel matrix computed from the training inputs, $\mathbf{k}_* \in \mathbb{R}^N$ is the kernel vector between the test input and the training inputs and $\mathbf{y} = [\hat{y}_1, \ldots, \hat{y}_n]^\top$ is the disturbance in the compensated form. After obtaining the GP prediction, the original disturbance d_g is recovered by adding the mean value of d_g back to the result:

$$\hat{d}_g = \bar{y}_* + \text{mean}(d_g), \tag{24}$$

This process ensures that the final prediction reflects the actual disturbance, including the compensation for the positive bias in the original dataset.

In this study, only the posterior mean $\bar{y}_*$ is used as the disturbance compensator. The posterior variance $\text{cov}(y_*)$ is not applied to the control input, but it is used in the analysis to provide a conservative bound on the disturbance estimate and is linked to the subsequent stability analysis. Accordingly, the proposed structure integrates the data-driven compensator with the DOB to address the DOB bandwidth/model-mismatch limits.

3.2. Performance and computational comparison of TISO -GPR kernels

In this section, the existing double squared exponential kernel (denoted as DS in (27)) is quantitatively compared with the proposed periodic + SE kernel (denoted as PS in (19)). The comparison provides the basis for kernel selection under operating changes by evaluating (i) in-domain prediction performance for $\mathcal{D}^{(1)}$–$\mathcal{D}^{(3)}$, (ii) extrapolation over the full position range, and (iii) the computational time from the view of the control cycle. This comparison clarifies the balance between performance and complexity under different levels of spatial coverage, and provides a quantitative basis for kernel selection.

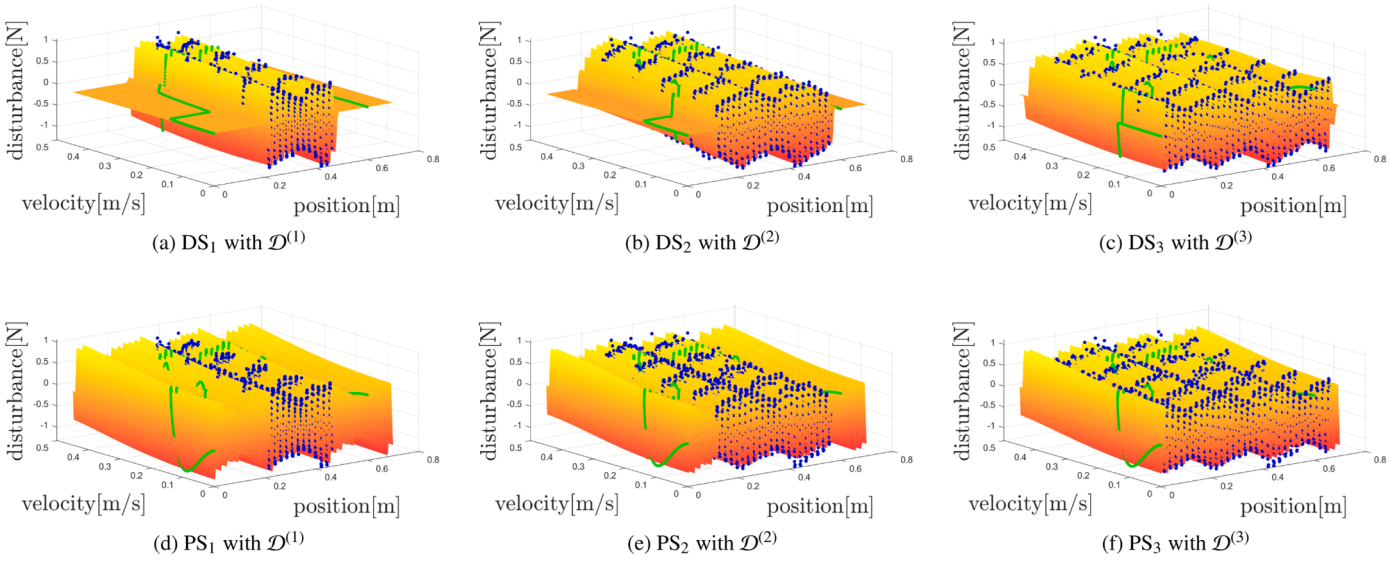

(a) DS_1 with $\mathcal{D}^{(1)}$ (b) DS_2 with $\mathcal{D}^{(2)}$ (c) DS_3 with $\mathcal{D}^{(3)}$

(d) PS_1 with $\mathcal{D}^{(1)}$ (e) PS_2 with $\mathcal{D}^{(2)}$ (f) PS_3 with $\mathcal{D}^{(3)}$

Fig. 6. TISO-GPR results with the DS kernels (a-c) and the PS kernels (d-f). Blue dots • indicate the training datasets $\mathcal{D}^{(1)}, \mathcal{D}^{(2)}$, and $\mathcal{D}^{(3)}$. The surfaces represent the posterior mean ■ inside each training region, and the green line — denotes the prediction along the full test trajectory. (For interpretation of the references to colour in this figure legend, the reader is referred to the web version of this article.)

To obtain the training data, the linear motor stage is operated repeatedly over the entire 700 mm range. The set of constant velocities is defined as $\mathcal{V} = v_1, \ldots, v_{10}$, and the center position of each constant-velocity section is defined as $x_{c,i}$. For each i, the training window is defined as

$$\mathcal{W}_k^{(i)} = \left[x_{c,i} - \frac{L_k}{2}, x_{c,i} + \frac{L_k}{2} \right], \tag{25}$$

$$L_k \in \{125, 225, 325\}\,\text{mm}, \tag{26}$$

where the spatial period is $\tau = 22.5$ mm, and the range lengths are set to $L_1 = 125$ mm, $L_2 = 225$ mm, and $L_3 = 325$ mm. For each velocity v_i, the position samples inside $\mathcal{W}_k^{(i)}$ and the constant velocity are paired to form the training data. The size of the final dataset is proportional to the range length and is defined as $\mathcal{D}^{(1)} \in \mathbb{R}^{1590}, \mathcal{D}^{(2)} \in \mathbb{R}^{2096}$, and $\mathcal{D}^{(3)} \in \mathbb{R}^{2460}$. Each dataset is downsampled beforehand due to the large volume of data, which would be too overwhelming to use for training the GP. The blue dots in Fig. 6 represent the training data. The kernel comparison is performed with the same $\mathcal{D}^{(k)}$, and the hyperparameters of each kernel are optimized independently using maximum a posteriori (MAP) estimation, which is based on the log marginal likelihood (LML) and prior knowledge of the hyperparameters in the kernel, as described in Section 3.3.

The comparison is performed with two kernels under the same TISO structure. The baseline model is the double squared exponential kernel ($\text{DS}_{\{1,2,3\}}$), and the proposed model is the periodic + SE kernel ($\text{PS}_{\{1,2,3\}}$) defined in (19). The kernel k^{ds} of the baseline DS model is expressed as follows.

$$k^{\text{ds}}(\mathbf{x}, \mathbf{x}') = k_x^{\text{se}}(x, x') + k_{\dot{x}}^{\text{se}}(\dot{x}, \dot{x}'). \tag{27}$$

where k_x^{se} and $k_{\dot{x}}^{se}$ are SE kernels with separated signal variances and length scales for the position and velocity axes. This DS kernel provides stable interpolation inside the trained region, whereas the posterior mean tends to zero outside the training range because the SE kernel approaches zero as the distance between inputs increases. As a result, the spatial periodic pattern on the position axis is not preserved outside the trained range, which requires dense coverage over the entire operating domain to achieve compensation over the full position range.

Fig. 6 shows the TISO-GPR results of (DS_1, DS_2, DS_3) and (PS_1, PS_2, PS_3) for the three training datasets $\mathcal{D}^{(1)}, \mathcal{D}^{(2)}$, and $\mathcal{D}^{(3)}$. The blue dots indicate the training data samples used for inference, and each surface represents the posterior mean evaluated over the full input domain. The green line represents the inference results for the entire test trajectory that includes the region outside the training range. These results allow the prediction characteristics obtained with the two kernels to be compared inside and outside the training range.

Table 1
RMSE between the measured disturbance over the full operating range and the GPR prediction trained with $\mathcal{D}^{(1)}, \mathcal{D}^{(2)}$, and $\mathcal{D}^{(3)}$.

Kernel	$\mathcal{D}^{(1)}$	$\mathcal{D}^{(2)}$	$\mathcal{D}^{(3)}$
DS	0.3789	0.2840	0.1550
PS	0.1516	0.1506	0.1493

Fig. 6. (a), (b), and (c) show the results of the TISO-GPR with the DS kernel trained with $\mathcal{D}^{(1)}, \mathcal{D}^{(2)}$, and $\mathcal{D}^{(3)}$, respectively. The posterior-mean surface accurately predicts the behavior of the sample data within the training range, confirming stable inference performance of the DS kernel. Outside the training range, however, the position-dependent kernel values converge to zero due to the absence of training data, and the prediction therefore depends solely on the posterior mean induced by the velocity component. This behavior arises because the SE kernel yields kernel values that decay toward zero as $|x - x'| \to \infty$, causing the posterior mean to become negligible when the distance between the training and test points becomes large.

Fig. 6. (d), (e), and (f) show the results of the TISO-GPR with the PS kernel trained with different datasets. Inside the training range, the posterior-mean surface predicts the behavior of the sample data in a stable manner, and a level of accuracy similar to that of the DS kernel is maintained. However, in the position region outside the training range, the periodic component in the PS kernel remains active. As a result, the predicted mean exhibits a spatial periodic pattern, and the position-dependent disturbance profile appears at positions that are not included in the training data. This confirms that effective estimation over the entire position range is possible even when the available training data cover only a limited region of the position axis. However, the velocity axis is based on the SE kernel, and the trained minimum-maximum velocity range is required to ensure reliable inference.

Table 1 shows that PS maintains a similar full-range RMSE across $\mathcal{D}^{(1)}$–$\mathcal{D}^{(3)}$, whereas DS improves only with denser coverage. Outside

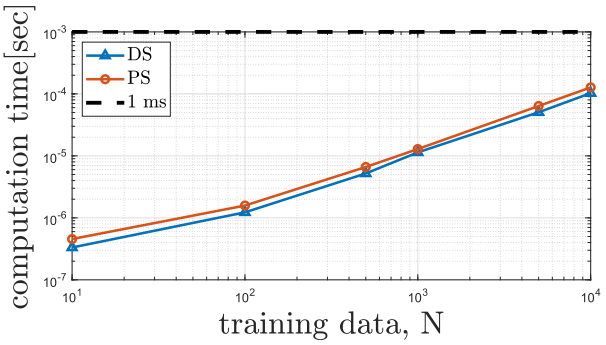

Fig. 7. Computation time per prediction versus dataset size N.

the training range, the PS kernel preserves the spatial periodic pattern, which provides consistent prediction on the position axis with a small coverage of training data. The velocity axis is based on the SE kernel, and reliable inference is ensured only inside the trained velocity range, which is used in the experiment.

The computational cost of GPR training is dominated by the Cholesky factorization of the kernel matrix. The training cost is $\mathcal{O}(N^3)$, and the memory usage is $\mathcal{O}(N^2)$. The inference uses the inner product between the kernel vector $\mathbf{k}_*$ and the precomputed vector $\boldsymbol{\alpha} = (\mathbf{K} + \sigma_n^2\mathbf{I})^{-1}\mathbf{y}$, and the per-query cost is $\mathcal{O}(N)$. The two kernels (DS and PS) require linear-algebra operations of the same order, and the computation time increases at a similar rate with respect to the number of data points N. The $\sin(\cdot)$ term in the position kernel of PS is negligible compared with the total cost and does not affect the computation time.

Fig. 7 shows how the per-query prediction time increases with the data size N on a logarithmic scale. The two curves almost overlap, and the observed slope follows a logarithmic pattern, which confirms the $\mathcal{O}(N)$ behavior in the measurement. While both kernels satisfy the real-time constraint at the current data size, Table 1 clearly shows that PS attains the desired performance with significantly fewer training samples. Therefore, the practical advantage of PS is data efficiency rather than computational speed.

3.3. Hyperparameter optimization and training visualization

The hyperparameters of the TISO-GPR model are determined by using MAP estimation (Sparacino et al., 2000). The parameter set is defined as $\theta = [\sigma_{f,x}, \ell_x, \sigma_{f,\dot{x}}, \ell_{\dot{x}}, \sigma_n]$, and the spatial period τ is fixed by the motor geometry. The MAP objective is defined as

$$J_{MAP} = J_{LML} + J_{prior} \tag{28}$$

where J_{LML} and J_{prior} are given by

$$J_{LML} = \log p(\mathbf{y}|\mathbf{X}, \theta) = -\frac{1}{2}\mathbf{d}^\top \left(\mathbf{K} + \sigma_n^2\mathbf{I}\right)^{-1}\mathbf{d} - \frac{1}{2}\log\left|\mathbf{K} + \sigma_n^2\mathbf{I}\right|, \tag{29}$$

When only J_{LML} is used, the optimization can converge to overly large or small values. Therefore, J_{prior} is defined as

$$J_{prior}(\boldsymbol{\phi}, \boldsymbol{\psi}) = (\theta - \boldsymbol{\phi})^\top \mathbf{P}^{-1}(\theta - \boldsymbol{\phi}), \tag{30}$$

where $\boldsymbol{\phi} \in \mathbb{R}^5$ represents the prior mean for each hyperparameter, $\boldsymbol{\psi} \in \mathbb{R}^5$ denotes the prior variance, and $\mathbf{P} \in \mathbb{R}^{5\times5} = \mathrm{diag}(\boldsymbol{\psi})$ is the diagonal prior covariance matrix. The prior parameters are set from the physical scales of $x, \dot{x}$, and the DOB-estimated disturbance, and the prior variances are selected to be weakly informative. For reproducibility, the hyperparameter estimation is performed under fixed prior parameters and the same training data.

The optimized hyperparameters are obtained offline and are fixed inside the controller. The prediction results in Fig. 6 are computed using independently optimized hyperparameters for each dataset.

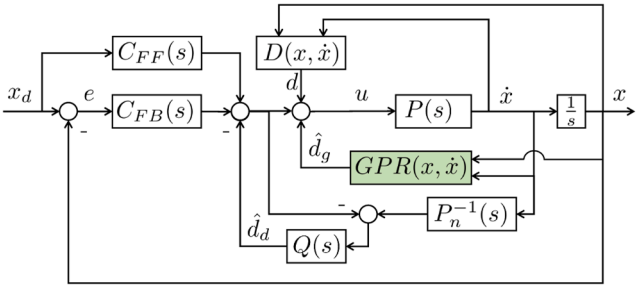

Fig. 8. Block diagram of the integrated controller.

4. Control architecture and stability analysis

4.1. Integration of GPR-based disturbance compensation into DOB framework

Fig. 8 shows the proposed control architecture based on a conventional two-degree-of-freedom (2-DoF) controller. A data-driven disturbance compensation based on the GPR is embedded inside the inner loop of the Disturbance Observer (DOB) so that it forms an additional compensation path within the DOB structure.

The integrated control includes four controllers: 1) feedforward control with $C_{\mathrm{FF}}(s)$, 2) feedback control with $C_{\mathrm{FB}}(s)$, 3) disturbance observer with $Q(s)$, $P_n(s)$, and 4) GPR-based compensator GPR. The feedforward controller is designed on the nominal rigid model $P_n(s)$ so that an immediate response to the position command is achieved:

$$C_{\mathrm{FF}}(s) = P_n^{-1}(s) = M_n s^2 + B_n s, \tag{31}$$

where M_n denotes the nominal mass and B_n denotes the nominal viscous term. On the other hand, the feedback control is designed as a proportional-derivative (PD) controller , $C_{\mathrm{FB}}(s)$, as given in (3), so that the position error is driven to zero.

The DOB is designed on the rigid model $P_n(s)$ and the Q-filter. The Q-filter $Q(s)$, given in (5), is implemented as a second-order filter.

The GP-based compensator is not expressed as an s-domain transfer function but as a Bayesian-based scheme in the time domain, represented by the posterior mean of the TISO GPR.

$$\hat{d}_g(t) = \mu(x(t), \dot{x}(t)), \tag{32}$$

where $\mu(x(t), \dot{x}(t))$ is given by (22). Therefore, $x_d(t), x(t) = \mathcal{P}u(t) + d(t)$, and $e(t) = x_d(t) - x(t)$ in Fig. 8 represent the position command, the measured position, and the position error, respectively. The term d denotes an unexpected disturbance caused by the position and velocity of the system, and the control rule u of the integrated controller is expressed as follows.

$$u(t) = u_{\mathrm{ff}}(t) + u_{\mathrm{fb}}(t) - \hat{d}_d(t) - \hat{d}_g(t), \tag{33}$$

where $u_{\mathrm{ff}}(t) = M_n\ddot{x}_d(t) + B_n\dot{x}_d(t), u_{\mathrm{fb}}(t) = K_d\dot{e}(t) + K_p e(t)$, and $\hat{d}_d(t) = \mathcal{Q}\left(\mathcal{P}_n^{-1}x(t) - u(t)\right)$ represent the control effort of the feedforward and feedback controllers, and the estimated disturbance of the disturbance observer, respectively. The operators $\mathcal{P}, \mathcal{P}_n$, and $\mathcal{Q}$ denote the time-domain representations of $P(s)$, $P_n(s)$, and $Q(s)$, respectively.

This structure is designed so that GPR-based compensation is applied as a real-time estimation of disturbances. The issues of modeling error and bandwidth setting in the conventional control configuration are reduced. In particular, the GPR compensation path is updated in the control input based on the currently measured state variables.

4.2. Robust stability analysis

In this section, robust stability of the closed-loop system is analyzed when the GPR-based disturbance compensation is included in the DOB inner loop. The analysis is carried out in the time domain by using linear operators and $\mathcal{L}_1$ norms. Under Assumptions 1-5, the outputs of the DOB

and the GPR compensator are first bounded (Lemmas 1 and 2). These bounds lead to a BIBO stability condition expressed by $\rho < 1$ and provide a design inequality for the GPR compensation gain.

4.2.1. Boundedness of GPR output

In this paper, two kernels for position and velocity are defined and combined as an additive kernel that $k(\mathbf{x}, \mathbf{x}') = k_x(x, x') + k_{\dot{x}}(\dot{x}, \dot{x}')$. In this kernel structure, the bounded property of the GPR prediction mean $\mu_p(\mathbf{x}_t)$ is shown by analyzing the relation of each term.

First, the position-based periodic kernel k_x has the limit property when the difference from the given training data $x_l(j)$ satisfies the periodic condition or when $\ell_x^2 \to 0$.

$$\lim_{\ell_x^2 \to 0} k_x(x_t, x_l(j)) = \begin{cases} \sigma_{f,x}^2 & \text{if } x_t - x_l(j) = k\tau, \\ 0 & \text{if } x_t - x_l(j) = \frac{(2k+1)\tau}{2}, \end{cases} \tag{34}$$

Therefore, when the position offset satisfies the periodic condition, that is $x_t - x_l(j) = k\tau$ or $(2k+1)\tau/2$, the kernel value converges to $\sigma_{f,x}^2$ or 0, respectively.

Consequently, each entry of the kernel matrix is bounded in $0 \le k_x(x_t, x_l(j)) \le \sigma_{f,x}^2$.

The posterior mean is expressed as $\mu(x_t) = k_{x,*}^\top \alpha + k_{\dot{x},*}^\top \alpha$. Thus, $\mu_x = k_{x,*}^\top \alpha$ and $\mu_{\dot{x}} = k_{\dot{x},*}^\top \alpha$. By Hölder's inequality, the following bound holds:

$$|k_{x,*}^\top \alpha| \le \|k_{x,*}\|_\infty \, \|\alpha\|_1. \tag{35}$$

Since $|k_{x,*}(j)| \le \sigma_{f,x}^2$ for all j, it follows that

$$\|k_{x,*}\|_\infty \le \sigma_{f,x}^2, \tag{36}$$

and the position-dependent part of the mean satisfies

$$|\mu_{p,x}(x_t)| \le \sigma_{f,x}^2 \|\alpha\|_1, \qquad 0 \le \sigma_x^2(x_t) \le \sigma_{f,x}^2. \tag{37}$$

In addition, the velocity-dependent squared exponential kernel $k_{\dot{x}}$ converges to 0 when the difference between inputs becomes infinitely large, and its maximum value is limited by the signal variance:

$$\lim_{|\dot{x}_t - \dot{x}_l(j)| \to \infty} k_{\dot{x}}(\dot{x}_t, \dot{x}_l(j)) = 0, \tag{38}$$

and its elementwise upper bound is:

$$0 \le k_{\dot{x}}(\dot{x}_t, \dot{x}_l(j)) \le \sigma_{f,\dot{x}}^2, \tag{39}$$

this bound directly leads to:

$$|k_{\dot{x},*}^\top \alpha| \le \|k_{\dot{x},*}\|_\infty \|\alpha\|_1 \le \sigma_{f,\dot{x}}^2 \|\alpha\|_1. \tag{40}$$

Accordingly, the prediction mean of the GPR output is bounded as

$$|\mu(\mathbf{x}_t)| \le \sigma_{f,x}^2 \|\alpha\|_1 + \sigma_{f,\dot{x}}^2 \|\alpha\|_1. \tag{41}$$

The overall bound can be written compactly as

$$|\mu(\mathbf{x}_t)| \le \left(\sigma_{f,x}^2 + \sigma_{f,\dot{x}}^2\right) \|\alpha\|_1. \tag{42}$$

This bounded property ensures that the magnitude of the GPR-based compensation term remains finite inside the DOB inner loop, which supports the stability analysis of the closed-loop system.

4.2.2. Closed-loop robust stability

When the closed-loop sensitivity operator $\mathcal{S}$, the disturbance path $\mathcal{G}_{d\to x}$, and the command path $\mathcal{G}_{x_d \to x}$ are defined in the time domain, they are given as:

$$\mathcal{S} = \mathcal{L}^{-1}\{S(s)\}, \tag{43}$$

$$\mathcal{G}_{d\to x} = \mathcal{S} \circ \mathcal{P} = \mathcal{L}^{-1}\{S(s)P(s)\} \tag{44}$$

$$\mathcal{G}_{x_d \to x} = \mathcal{T} + \mathcal{S} \circ \mathcal{P} \circ \mathcal{C}_{\mathrm{FF}}, \tag{45}$$

Based on these equations, the closed-loop output x is expressed as:

$$x = \mathcal{G}_{d\to x}\{\, d - \hat{d}_d - \hat{d}_g \,\} + \mathcal{G}_{x_d \to x}\, x_d, \tag{46}$$

Note that the linear operator $\mathcal{G}_{d\to x}$ for the disturbance component is separated. This separation enables the disturbance effect to be analyzed independently, and the bounded property of the GPR output supports the stability analysis.

Assumption 1. The inner loop composed of $\mathcal{P}$ and C_{FB} is stable. For the disturbance and reference path operators, it holds that $\gamma_{d\to x} = \|\mathcal{G}_{d\to x}\|_1 < \infty$ and $\gamma_{x_d \to x} = \|\mathcal{G}_{x_d \to x}\|_1 < \infty$.

Assumption 2. The operators $\mathcal{Q}, \mathcal{F}_{\dot{x}}$, and $\mathcal{Q} \circ \mathcal{P}_n^{-1}$ are stable. The constants are defined as $\gamma_q := \|\mathcal{Q} \circ \mathcal{P}_n^{-1}\|_1$ and $\gamma_{\dot{x}} := \|\mathcal{F}_{\dot{x}}\|_1$. The velocity is implemented as $\dot{x} = \mathcal{F}_{\dot{x}}(x)$.

Assumption 3. The position command x_d and the disturbance d are assumed to be bounded signals.

It is important to note that the posterior mean function μ in (22) is a linear combination of kernel sections as

$$\mu(x, \dot{x}) = \sum_{i=1}^{N} c_i k(\mathbf{x}, \mathbf{x}_i) = \sum_{i=1}^{N} c_i \left(k_x(x, x_i) + k_{\dot{x}}(\dot{x}, \dot{x}_i)\right)$$

for some constants $c_i, i = 1, \ldots, N$. Since both kernels k_x and $k_{\dot{x}}$ in (20) and (21) are locally Lipschitz on the training domain $\mathcal{X}$, there exist nonnegative constants L_x and $L_{\dot{x}}$ such that

$$|\mu(x_1, \dot{x}_1) - \mu(x_2, \dot{x}_2)| \le L_x |x_1 - x_2| + L_{\dot{x}} |\dot{x}_1 - \dot{x}_2|. \tag{47}$$

for any $[x_1, \dot{x}_1]^\top, [x_2, \dot{x}_2]^\top \in \mathcal{X}$. In addition, the regression error is assumed to be bounded on $\mathcal{X}$ as stated in Assumption 4.

Assumption 4. There exists a bias upper bound $b_\mu \ge 0$ for the lumped disturbance such that

$$|\mu(x, \dot{x}) - d(x, \dot{x})| \le b_\mu \quad \forall [x, \dot{x}]^\top \in \mathcal{X}. \tag{48}$$

It is well-known from (Lederer et al., 2019; Srinivas et al., 2009) that error bounds for GPR are typically given in a stochastic form, depending on the posterior variance function and the reproducing kernel Hilbert space norm of the target function. In this paper, the stability analysis is developed by using a uniform bound b_μ on the regression error over the compact domain $\mathcal{X}$, and such a bound can be constructed from the posterior variance as described in Remark 1.

Remark 1. Let $\Pr\{\cdot\}$ denote the probability induced by the GP prior and the measurement noise model. For a given $\delta \in (0, 1)$ and $\beta_\delta > 0$ on a compact domain $\mathcal{X}$, a standard high-probability error bound of GPR is given as:

$$\Pr\left\{|\mu(x, \dot{x}) - d(x, \dot{x})| \le \beta_\delta \sigma(x, \dot{x}), \forall [x, \dot{x}]^\top \in \mathcal{X}\right\} \ge 1 - \delta, \tag{49}$$

where $\sigma(x, \dot{x})$ is the posterior standard deviation. Accordingly, a uniform bound in Assumption 4 can be constructed as

$$b_\mu := \sup_{[x,\dot{x}]^\top \in \mathcal{X}} \beta_\delta \sigma(x, \dot{x}). \tag{50}$$

Therefore, the term b_μ in Lemma 2 can be evaluated from the posterior variance (via σ), which provides a conservative bound in the stability analysis over $\mathcal{X}$.

Remark 2. The DOB estimate is written as

$$\hat{d}_d = \mathcal{Q} \circ \mathcal{P}_n^{-1}\{x\} - \mathcal{Q}\{u\}. \tag{51}$$

Since the inner loop composed of $\mathcal{P}$ and C_{FB} is stable, it holds that

$$\|u\|_\infty \le \gamma_{x\to u} \|x\|_\infty + c_u, \tag{52}$$

for some finite constants $\gamma_{x\to u} \ge 0$ and $c_u \ge 0$.

Assumption 5. The GPR compensation is implemented through a weighting factor and a low-pass filter:

$$\hat{d}_g = \mathcal{F}_{gp}\{\alpha(t)\, \mu(x, \dot{x})\}, \qquad 0 \le \alpha(t) \le \alpha_{\max} < 1, \tag{53}$$

where $\gamma_g = \|\mathcal{F}_{gp}\|_1$. The filter $\mathcal{F}_{gp}$ is strictly proper so that no algebraic loop occurs.

Lemma 1 (DOB bound). *For all time t, the output of the DOB is bounded as*

$$\|\hat{d}_d\|_\infty \le \gamma_q \|x\|_\infty + \gamma_q \|u\|_\infty, \tag{54}$$

where γ_q is defined in Assumption 2.

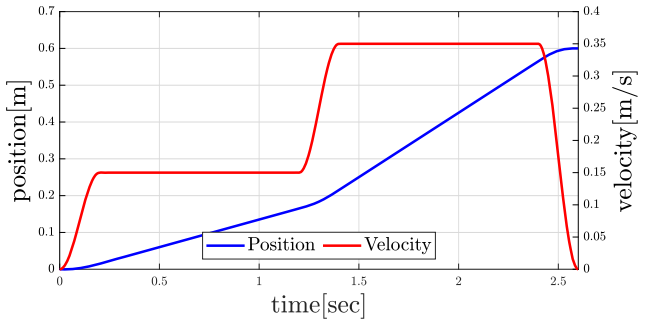

Fig. 9. Reference position and velocity profile.

Lemma 2 (GPR bound). *The output of the GPR is upper bounded for all time t by Young's convolution inequality:*

$$\|\hat{d}_g\|_\infty \le \gamma_g \alpha_{\max}(L_x\|x\|_\infty + L_{\dot{x}}\|\dot{x}\|_\infty + b_\mu)$$
$$\le \gamma_g \alpha_{\max}((L_x + L_{\dot{x}}\gamma_{\dot{x}})\|x\|_\infty + b_\mu) \quad (55)$$
$$\le \gamma_g \alpha_{\max}(K\|x\|_\infty + b_\mu), \quad (56)$$

where $K = L_x + L_{\dot{x}}\gamma_{\dot{x}}$.

By using Lemmas 1 and 2 with (52), the following inequality is obtained from (46):

$$\|x\|_\infty \le \rho\,\|x\|_\infty + c_d\|d\|_\infty + c_r\|x_d\|_\infty + c_0, \quad (57)$$

where the constants are defined as

$$\rho := \gamma_{d\to x}\big(\gamma_q(1+\gamma_{x\to u}) + \gamma_g\alpha_{\max}K\big), \quad (58)$$
$$c_d := \gamma_{d\to x}, \qquad c_r := \gamma_{x_d\to x}, \quad (59)$$
$$c_0 := \gamma_{d\to x}\big(\gamma_q c_u + \gamma_g\alpha_{\max}b_\mu\big). \quad (60)$$

Proposition 1 (BIBO stability). *If $\rho < 1$ holds, the system is BIBO stable. In addition, the output is bounded as*

$$\|x\|_\infty \le \frac{c_d\|d\|_\infty + c_r\|x_d\|_\infty + c_0}{1-\rho}. \quad (61)$$

A sufficient condition for $\rho < 1$ is given by

$$\alpha_{\max} < \frac{\frac{1}{\gamma_{d\to x}} - \gamma_q(1+\gamma_{x\to u})}{\gamma_g K}, \quad (62)$$

where $\frac{1}{\gamma_{d\to x}} > \gamma_q(1+\gamma_{x\to u})$ is required to ensure that the right-hand side remains positive, and $\gamma_q(1+\gamma_{x\to u})$ represents the DOB-related loop gain.

5. Experimental result

5.1. Experimental setup

In this section, the performance of the integrated control that includes the proposed TISO-GPR is experimentally verified as shown in Fig. 8. The design parameters of the feedback, feedforward, and DOB are fixed in all comparisons so that the effect of the disturbance and the behavior outside the training range is evaluated independently. The proposed TISO-GPR is located inside the DOB loop, and the TISO-GPR is executed at each control sampling time in real time.

The target stage is the core-type single-axis linear motor in Fig. 1 (model: Kovery 2P-06), and the encoder resolution is 0.2 μm. The control algorithm is executed with the Quanser QPIDe board at the control period of 1 ms. The command used in the experiment is the position and velocity command in Fig. 9, and the stage moves from 0 mm to 600 mm. This command includes two constant-velocity sections, and the constant velocities are 150 mm/s and 350 mm/s. The acceleration and deceleration are set to signals that increase smoothly using a sinusoidal signal, and this profile is designed so that position-based and velocity-dependent disturbances can be observed under both low-speed and high-speed conditions.

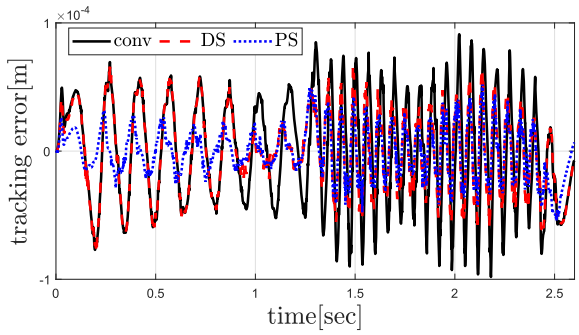

Fig. 10. Closed-loop tracking error under the three control conditions.

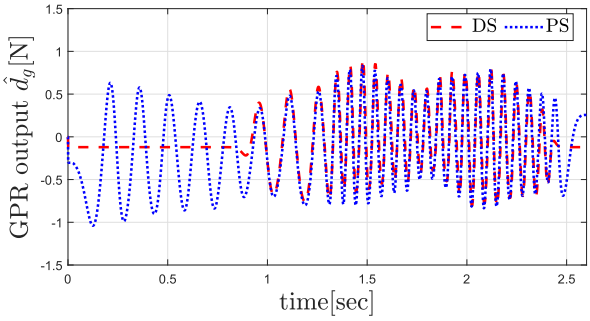

Fig. 11. Disturbance estimates obtained from the GPR-based compensator under the three control conditions.

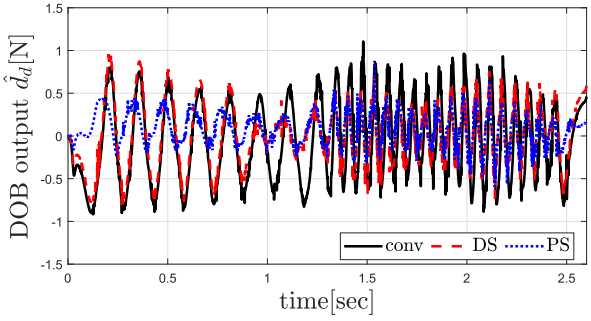

Fig. 12. DOB output under the three control conditions.

The dataset $D^{(2)}$ defined in Section 3.2 is used for training. The hyperparameters are optimized in an offline process and are fixed in all experiments. In Section 5.2, the closed-loop performance is compared by changing the kernel setting inside the TISO-GPR while the remaining controller settings are fixed. In Section 5.3, an additional mass is attached to the moving carrier of the linear motor to generate model uncertainty intentionally and conditions outside the training range, and it is verified that the proposed integrated control operates in a robust manner without retraining.

5.2. Performance comparison among the three control approaches

In this section, the performance of the proposed TISO-GPR-based integrated control is experimentally compared under different conditions. The compared cases are the DOB structure, which is the structure without the GPR in Fig. 8, the TISO-GPR with the DS kernel, and the TISO-GPR with the PS kernel. The parameters of the FF, FB, and DOB are fixed in all cases so that the result is affected by the selected kernel and the disturbance model. The command reference is shown in Fig. 9.

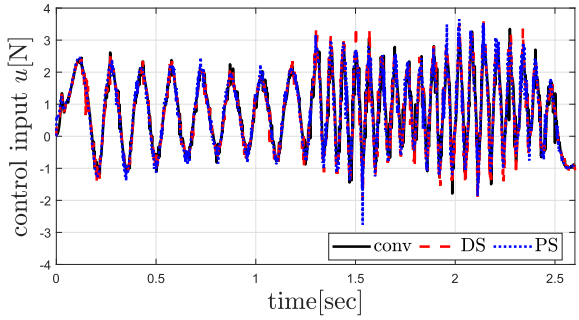

Fig. 13. Control inputs generated under the three control conditions.

Fig. 10 is the position tracking error when the command trajectory in Fig. 9 is applied. The black solid line shows the error of the conventional FF/FB/DOB structure without the TISO-GPR. The red dashed line shows the error of the proposed control in which the TISO-GPR with the DS kernel is used. The blue dotted line shows the error of the proposed control in which the TISO-GPR with the PS kernel is used.

The conventional controller shows the largest tracking error in all sections. The DS and PS cases show smaller errors than the conventional controller because the TISO-GPR compensates the trained disturbance inside the DOB loop. An error close to the conventional case is observed in the DS case outside the training range. Inside the training range, the DS case shows a smaller error than the conventional case because the disturbance is compensated by the TISO-GPR inside the DOB loop, although the error of the DS case is larger than the PS case in the same region.

The PS case shows a smaller error than the conventional controller even outside the training range. This result is obtained because the PS kernel reflects the spatial period so that the spatial pattern of the disturbance is estimated even in the untrained region. Inside the training range, the PS case also maintains a smaller error than the DS case, and this result indicates that the PS-based estimation provides stable compensation for the entire spatial disturbance. The results are summarized in Table 2.

Fig. 11 shows the GPR-based disturbance estimate $\hat{d}_g$ generated in the DS and PS cases. The DS case produces values that converge to a fixed value outside the training range, as shown in Fig. 6(a)-(c). This behavior is obtained because the DS kernel is defined so that the disturbance is represented inside the trained region. Therefore, the DS case does not estimate the disturbance in the untrained region. In contrast, the PS case produces outputs in the untrained region. This behavior is obtained because the PS kernel is defined with the spatial period, and the spatial periodicity of the disturbance is preserved when the input of the TISO-GPR is outside the training range. Therefore, the PS case continuously estimates the spatial pattern of the disturbance over the entire region, and the position-based disturbance property is inferred outside the training range.

Fig. 12 shows the DOB output $\hat{d}_d$ generated, as shown in Fig. 8. In the conventional case, the TISO-GPR is not included, and the disturbance compensation is fully dependent on the DOB. Therefore, the DOB output becomes larger than in the DS and PS cases. In contrast, The DS case shows a DOB output close to the conventional case when the position is outside the training domain because the DS kernel becomes inactive in that region, and the DOB performs the compensation. Inside the training range, the GPR compensates the disturbance ahead of the DOB, and the DOB output decreases.

The PS case produces TISO-GPR outputs in the untrained region, and the DOB output remains lower than the conventional case throughout the experiment. This behavior is obtained because the PS kernel estimates the spatial pattern of the disturbance even outside the training range, and the load of the DOB remains reduced over the entire region.

Table 2
Tracking error RMSE under the three control conditions.

	conv	DS	PS
RMSE [μm]	42.048	29.228	22.408

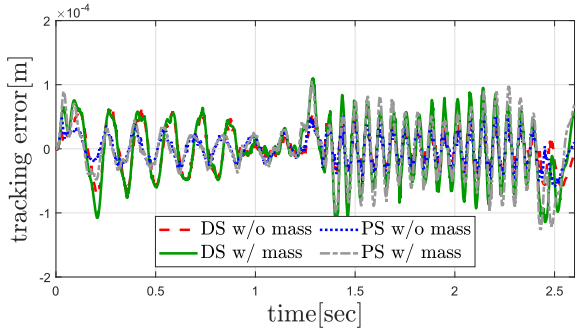

Fig. 14. Closed-loop tracking error with and without the additional mass.

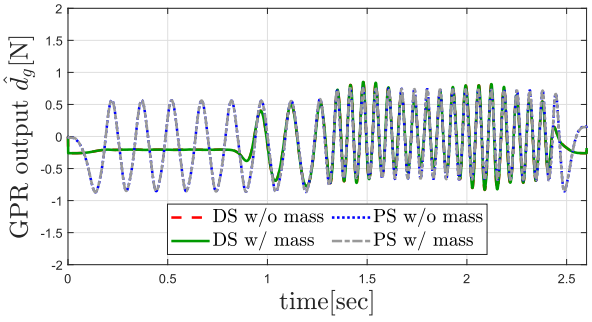

Fig. 15. GPR-based disturbance estimates with and without the additional mass.

Fig. 13 shows the total control input u in Fig. 8 applied to the plant in the three cases. The magnitude and pattern of the control input are similar across all cases (DOB, DS, and PS), indicating that incorporating the TISO-GPR into the DOB loop does not result in an excessive increase in control effort. In the DS case, disturbance estimation outside the training range is carried out by the DOB, leading to control behavior comparable to that of the conventional DOB.

Within the training range, the TISO-GPR compensates for the disturbance and reduces the DOB output, yet without increasing the total control input. In the PS case, disturbance estimation is performed over the entire operating range, which further decreases the DOB output; however, the overall control input remains comparable to the other cases. Overall, the proposed TISO-GPR-based integrated control enhances disturbance compensation performance while maintaining a control input level similar to that of the conventional DOB-based structure.

5.3. Robustness evaluation under payload variation

The experiments in Section 5.2 are carried out based on the identified nominal model. The DOB $P_n(s)$ and the feedforward $C_{FF}(s)$ are set with the same model parameters, and the main uncertainty is assumed to be limited to the velocity-dependent viscous friction. Therefore, the performance of the TISO-GPR with the DS and PS kernels is verified when the mass parameter is assumed to be accurate.

In this section, an additional mass 21 kg is attached to the moving carrier so that this assumption is intentionally violated. The parameters M_n and B_n of $C_{FF}(s)$ and $P_n(s)$ are not modified although the mass is increased, and this condition produces a mismatch between the nominal model and the real system. In Figs. 14–17, the red dashed and blue

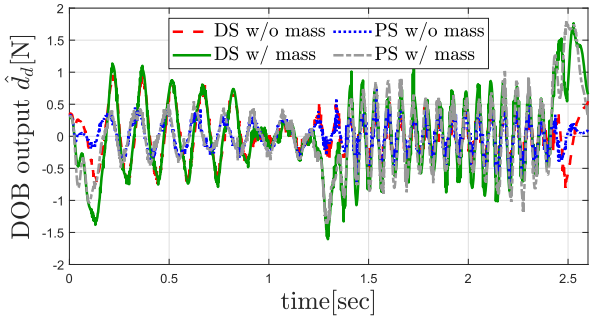

Fig. 16. Disturbance observer output with and without the additional mass.

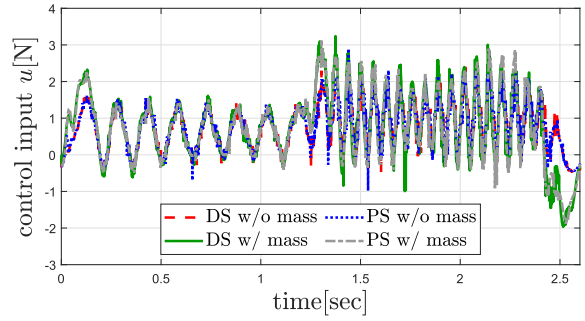

Fig. 17. Control input with and without the additional mass.

dotted lines denote the DS and PS cases without the additional mass, and the green solid and gray dash-dotted lines denote the DS and PS results with the additional mass, respectively.

Fig. 14 shows that the tracking error increases under the additional-mass condition, especially in the high–acceleration and deceleration intervals, including 0.0~0.2, 1.2~1.4, and 2.4 ~ 2.6 s. The overall error trend remains similar between the DS and PS cases, while larger peak errors appear during the transient intervals. This behavior is explained by analyzing the components of the control input.

Fig. 15 shows that the disturbance estimate remains almost unchanged for both kernels under the additional-mass condition. The change in the mass parameter is not reflected in the learned model because the GPR is trained without the additional mass. Therefore, no additional compensation is generated for the mass mismatch, and the resulting model uncertainty is handled by the integrated structure.

Fig. 16 shows that larger DOB outputs appear during the acceleration and deceleration intervals under the additional-mass condition. This increase reflects the additional control effort required to compensate the inertia mismatch. Since the nominal mass is smaller than the actual value, the DOB generates a larger force to compensate the acceleration-dependent disturbance.

Fig. 17 shows that the total control input increases during the acceleration and deceleration intervals under the additional-mass condition, which is consistent with the increase in the DOB output. The larger input reflects the compensation required for the inertia mismatch introduced by the payload variation.

These results confirm that the integrated control preserves tracking performance and closed-loop stability under the payload variation. The GPR compensates the learned position- and velocity-dependent disturbance, while the DOB compensates the inertia mismatch that is not included in the training data. The combined action of the two components maintains robust performance under the additional-mass condition.

6. Conclusion

A control structure is proposed that adds the TISO-GPR-based disturbance compensation in parallel to the conventional DOB-based two-degree-of-freedom control. The lumped disturbance is modeled by using the position-velocity input, the periodic kernel on the position axis, and the SE kernel on the velocity axis, and the bounded property of the GPR compensation and the BIBO stability condition in a small-gain form are presented by the time-domain analysis.

The experiments show that the Periodic(x)+SE($\dot{x}$) TISO-GPR reduces the tracking error and the DOB output over the entire range while the control input is maintained when compared with the conventional FF/FB/DOB and the double-SE TISO-GPR. The performance is also maintained under the untrained condition, including the additional-mass case, and the proposed Gaussian Process-based integrated control provides improved performance and stability under the model mismatch and the change in the operating condition. Variance-aware compensation can be investigated as a future extension.

CRediT authorship contribution statement

Hanul Jung: Writing – review & editing, Writing – original draft, Visualization, Validation, Supervision, Methodology, Investigation, Funding acquisition, Formal analysis, Conceptualization; **Hoyeong Yeo:** Writing – review & editing, Visualization, Validation, Methodology, Formal analysis, Conceptualization; **Hamin Chang:** Writing – review & editing, Validation, Methodology, Conceptualization; **Sehoon Oh:** Writing – review & editing, Supervision, Funding acquisition, Formal analysis.

Declaration of competing interest

The authors declare that they have no known competing financial interests or personal relationships that could have appeared to influence the work reported in this paper.

References

Aarnoudse, L., Cox, K., Koekebakker, S., & Oomen, T. (2024). Multirate repetitive control for an industrial print-belt system. *Mechatronics*, *100*, 103187.

Ahmed, S., Grabher, C., Kim, H.-J., & Koseki, T. (2019). Multifidelity surrogate assisted rapid design of transverse-flux permanent magnet linear synchronous motor. *IEEE Transactions on Industrial Electronics*, *67*(9), 7280–7289.

Beckers, T., Seidman, J., Perdikaris, P., & Pappas, G.J. (2022). Gaussian process port-hamiltonian systems: Bayesian learning with physics prior. In *2022 IEEE 61st conference on decision and control (CDC)* (pp. 1447–1453). IEEE.

Cho, K., & Nam, K. (2021). Robust periodic adaptive disturbance observer based control considering long-term instability problems for high-load motion systems. *IEEE Transactions on Industrial Electronics*, *69*(6), 6258–6266.

Gao, H., Liu, Y., Sun, W., & Yu, X. (2023). Adaptive wavelet tracking control of dual-linear-motor-driven gantry stage with suppression of crossbeam rotation. *IEEE/ASME Transactions on Mechatronics*, *29*(1), 97–105.

Lederer, A., Umlauft, J., & Hirche, S. (2019). Uniform error bounds for Gaussian process regression with application to safe control. *Advances in Neural Information Processing Systems*, *32*.

Li, L., Huang, W.-W., Wang, X., Chen, Y.-L., & Zhu, L. (2022). Periodic-disturbance observer using spectrum-selection filtering scheme for cross-coupling suppression in atomic force microscopy. *IEEE Transactions on Automation Science and Engineering*, *20*(3), 2037–2048.

Li, X., Chen, S.-L., Teo, C. S., & Tan, K.K. (2017). Data-based tuning of reduced-order inverse model in both disturbance observer and feedforward with application to tray indexing. *IEEE Transactions on Industrial Electronics*, *64*(7), 5492–5501.

Liu, Z., Zhang, Z., Liu, Y., Li, W., Pan, H., & Sun, W. (2023). Neural networks-based adaptive control for linear motors with cogging force compensation. In *Iecon 2023-49th annual conference of the IEEE industrial electronics society* (pp. 1–6). IEEE.

Mooren, N., van Meer, M., Witvoet, G., & Oomen, T. (2024). Compensating torque ripples in a coarse pointing mechanism for free-space optical communication: A gaussian process repetitive control approach. *Mechatronics*, *97*, 103107.

Mooren, N., Witvoet, G., & Oomen, T. (2022). A Gaussian process approach to multiple internal models in repetitive control. In *2022 IEEE 17th international conference on advanced motion control (AMC)* (pp. 274–279). IEEE.

Rogers, E., Chu, B., Moore, K., Oomen, T., & Tan, Y. (2024). Iterative learning control-algorithms, applications and future research directions. In *2024 IEEE 63rd conference on decision and control (CDC)* (pp. 2252–2268). IEEE.

Sasaki, R., Ohnishi, W., Koseki, T., Sakata, K., Yang, P.-H., Keswani, G., & Kim, H.-J. (2024). State variable dependent disturbances compensation using gaussian process regression: With application to core-type linear motor. In *2024 IEEE international conference on advanced intelligent mechatronics (AIM)* (pp. 416–421). IEEE.

Sparacino, G., Tombolato, C., & Cobelli, C. (2000). Maximum-likelihood versus maximum a posteriori parameter estimation of physiological system models: The c-peptide impulse response case study. *IEEE Transactions on Biomedical Engineering*, *47*(6), 801–811.

Srinivas, N., Krause, A., Kakade, S.M., & Seeger, M. (2009). Gaussian process optimization in the bandit setting: No regret and experimental design. arXiv:0912.3995.

Tan, K.K., Lee, T.H., Dou, H., & Zhao, S. (2004). Force ripple suppression in iron-core permanent magnet linear motors using an adaptive dither. *Journal of the Franklin Institute*, *341*(4), 375–390.

Topa, H., Jónás, Á., Kofler, R., Kosiol, C., & Honkela, A. (2015). Gaussian process test for high-throughput sequencing time series: Application to experimental evolution. *Bioinformatics*, *31*(11), 1762–1770.

Tsurumoto, K., Ohnishi, W., Koseki, T., Van Haren, M., & Oomen, T. (2024). Integrated rational feedforward in frequency-domain iterative learning control for highly task-flexible motion control. *IEEE/ASME Transactions on Mechatronics*, *29*(4), 3010–3018.

Wang, L., Zhao, J., Yu, Z., Pan, Z., & Zheng, Z. (2024). Robust and high-precision position control of PMLSM-driven feed servo system based on adaptive fast nonsingular terminal sliding mode. *IEEE Transactions on Transportation Electrification 11*(1), 4882–4894.

Wang, M., Kang, K., Zhang, C., & Li, L. (2023). Precise position control in air-bearing PMLSM system using an improved anticipatory fractional-order iterative learning control. *IEEE Transactions on Industrial Electronics*, *71*(6), 6073–6083.

Wu, L., Chen, H., Mao, Y., Ye, X., & Kang, R. (2024a). Robustness-oriented design optimization approach for cogging torque of batch production PMSM. *IEEE Transactions on Energy Conversion*, *39*(3), 1711–1725.

Wu, L., Li, Y., & Lu, Q. (2024b). Detent force fast optimization method of modular permanent-magnet linear synchronous motors. *IEEE Transactions on Industrial Electronics*, *71*(12), 16191–16199.

Yang, X., & Zhou, Y. (2023). Pm flux analysis and thrust density enhancement of a transverse-flux-reversal linear motor for transportation system. *IEEE Transactions on Transportation Electrification*, *10*(3), 5294–5306.